

See discussions, stats, and author profiles for this publication at: <https://www.researchgate.net/publication/5462913>

# Investigation of Short-Term Changes in Visual Evoked Potentials With Windowed Adaptive Chirplet Transform

Article in IEEE transactions on bio-medical engineering · May 2008

DOI: 10.1109/TBME.2008.918439 · Source: PubMed

CITATIONS

20

READS

79

2 authors, including:



Richard J. Cui

Barrow Neurological Institute

31 PUBLICATIONS 692 CITATIONS

SEE PROFILE

It has previously been shown that cells prefer to grow on pSi (better viability) as compared to smooth Si [1]–[3], but the pore size influence has not been investigated in detail and the majority of studies are made on pores smaller than 150 nm. Interestingly, Sapelkin *et al.* [4] showed that cell bodies of the neuronal B50-cell line showed clear adhesion preference on porous (50–100 nm average pore size) areas as compared to smooth Si surfaces. Our study indicates that axons have no such selectivity in this pore size range. It may therefore be hypothesized that the mechanism that make cell bodies attach to surfaces in an acute adhesion phase differs from the way axons attach during regeneration. Furthermore, Karlsson [13] found a lower activation of adherent neutrophils on  $\text{Al}_2\text{O}_3$  with 200-nm-wide pores as compared to 20-nm-wide pores, also indicating a lower optimal pore size for cell culturing.

For clinical applications, the pore size range may be revised for human axons since axon diameter may influence the results. In a recent study, we showed that nano-imprinted patterns could guide axons, but frequently, large axons were not guided, indicating an axon-diameter-dependent reaction to topographic cues [10]. For bio-implantation, pSi appears attractive. Axonal guidance and biocompatibility could be enhanced further by incorporate, e.g., growth factors on the surface. Due to the very large area/volume ratio of pSi, large amounts can be incorporated [14], improving neural survival and axonal sprouting. pSi is also suitable for other surface modifications that can promote cell viability and adhesion, although, cell reaction may change not only with surface topography/chemistry, but also with cell type [15]. Furthermore, the increased surface area of pSi makes it suitable as an electrode material with a large chip-cell contact area.

We finally conclude in this study that axons thrive on pSi and exhibit a haptotactic reaction within a certain range of 150–500 nm average pore diameter. This could be utilized to guide axons on chip surfaces.

#### ACKNOWLEDGMENT

The authors would like to thank I. Antonsson for expert technical assistance and Dr. A. Ressine, P. Gustavsson, and W. Hållström for their valuable discussions regarding pSi and axonal regeneration.

#### REFERENCES

- [1] S. C. Bayliss, L. D. Buckberry, I. Fletcher, and M. J. Tobin, "The culture of neurons on silicon," *Sens. Actuators A*, vol. 74, pp. 139–142, 1999.
- [2] S. C. Bayliss, L. D. Buckberry, P. J. Harris, and M. J. Tobin, "Nature of the silicon-animal cell interface," *J. Porous Mater.*, vol. 7, pp. 191–195, 2000.
- [3] S. C. Bayliss, R. Heald, I. Fletcher, and L. D. Buckberry, "The culture of mammalian cells on nanostructured silicon," *Adv. Mater.*, vol. 11, no. 4, pp. 318–321, 1999.
- [4] A. V. Sapelkin, S. C. Bayliss, B. Unal, and A. Charalambou, "Interaction of B50 rat hippocampal cells with stain-etched porous silicon," *Biomaterials*, vol. 27, pp. 842–846, 2006.
- [5] F. Johansson, M. Kanje, C. Eriksson, and L. Wallman, "Guidance of neurons on porous patterned silicon: Is pore size important?," *Physica Status Solidi C*, vol. 9, pp. 3258–3262, 2005.
- [6] A. Rosengren, L. Wallman, N. Danielsen, T. Laurell, and L. M. Bjursten, "Tissue reaction evoked by porous and plane surfaces made out of silicon and titanium," *IEEE Trans. Biomed. Eng.*, vol. 49, no. 4, pp. 392–399, Apr. 2002.
- [7] A. Angelescu, I. Kleporous silicon, M. Mihaela, M. Simion, T. Neghina, S. Petrescu, N. Moldovan, C. Paduraru, and A. Raducanu, "Porous silicon matrix for applications in biology," *Rev. Adv. Mater. Sci.*, vol. 5, pp. 440–449, 2003.
- [8] J. Drott, K. Lindström, L. Rosengren, and T. Laurell, "Porous silicon as the carrier matrix microstructured enzyme reactors yielding high enzyme activities," *J. Micromech. Microeng.*, vol. 7, pp. 14–23, 1997.
- [9] L. T. Canham, R. S. Saffie, S. E. Connor, and R. Aston, *Silicon Technology and Pharmaceuticals – An Impending Marriage in the Nanoworld*. London, U.K.: Drug Discovery World, 2001, pp. 56–63.
- [10] F. Johansson, P. Carlberg, N. Danielsen, L. Montelius, and M. Kanje, "Axonal outgrowth on nano-imprinted patterns," *Biomaterials*, vol. 27, pp. 1251–1258, 2006.
- [11] H. Föll, M. Christophersen, J. Carstensen, and G. Hasse, "Formation and application of porous silicon," *Mater. Sci. Eng.*, vol. 39, pp. 93–141, 2002.
- [12] E. Engvall and U. M. Wewer, "Domains of laminin," *J. Cell. Biochem.*, vol. 61, pp. 493–501, 1996.
- [13] M. Karlsson, A. Johansson, L. Tang, and M. Boman, "Nanoporous aluminium oxide affects neutrophil behaviour," *Microscopy Res. Tech.*, vol. 63, pp. 259–265, 2004.
- [14] L. M. Karlsson, P. Tengvall, I. Lundström, and H. Arwin, "Penetration and loading of human serum albumin in porous silicon layers with different pore sizes and thicknesses," *J. Colloid Interface Sci.*, vol. 266, pp. 40–47, 2003.
- [15] S. P. Low, K. A. Williams, L. T. Canham, and N. H. Voelcker, "Evaluation of mammalian cell adhesion on surface-modified porous silicon," *Biomaterials*, vol. 26, pp. 4538–4546, 2006.

## Investigation of Short-Term Changes in Visual Evoked Potentials With Windowed Adaptive Chirplet Transform

Jie Cui and Willy Wong\*

**Abstract**—We propose a new application of the adaptive chirplet transform that involves partitioning signals into non-overlapping sequential segments. From these segments, the local time-frequency structures of the signal are estimated by using a four-parameter chirplet decomposition. Entitled the windowed adaptive chirplet transform (windowed ACT), this approach is applied to the analysis of visual evoked potentials (VEPs). It can provide a unified and compact representation of VEPs from the transient buildup to the steady-state portion with less computational cost than its non-windowed counterpart. This paper also details a method to select the optimal window length for signal segmentation. This approach will be useful for long-term signal monitoring as well as for signal feature extraction and data compression.

**Index Terms**—Chirplet transform, optimal window length, short-term changes, time-frequency analysis, visual evoked potentials.

#### I. INTRODUCTION

VISUAL evoked potentials (VEPs) are surface electrical potentials measured from the scalp in response to a visual signal [1]. It is believed that they are generated from the visual cortex and/or the peripheral neural pathways leading to the cortex. One type of VEPs known as steady-state VEPs (ssVEPs) are usually established if the repetition rate of visual stimuli is sufficiently high (usually, above 6 times per second). In this case, the responses begin to merge and the shape of the resulting VEP becomes periodic.

ssVEPs not only have prominent clinical significance in helping diagnose sensory dysfunctions (e.g., [2], [3]), but also have found, more recently, application within interface design (e.g., [4], [5]). Accordingly, a number of studies have investigated the mechanism underlying

Manuscript received May 5, 2007; revised August 18, 2007. This work was supported in part by NSERC Canada. Asterisk indicates corresponding author.

J. Cui was with the Institute of Biomaterials and Biomedical Engineering, University of Toronto, 164 College Street, Toronto, ON, M5S 3G9, Canada. He is currently with the School of Health Information Sciences, University of Texas Health Science Center at Houston, 7000 Fannin Street, Suite 600, Houston, TX 77030 USA (e-mail: jie.cui@uth.tmc.edu).

\*W. Wong is with the Institute of Biomaterials and Biomedical Engineering, University of Toronto, Toronto, ON, M5S 3G9, Canada, and also with the Department of Electrical and Computer Engineering, University of Toronto, Toronto, ON, M5S 3G4, Canada (e-mail: willy@eecg.utoronto.ca).

Digital Object Identifier 10.1109/TBME.2008.918439

the formation of *ssVEPs* [6]–[8]. An important aspect of these investigations is the characterization of the time course of *ssVEP* responses, such as the variation of the amplitude and phase of the frequencies of interest, prior to and following visual stimulation. Previous studies have shown that time is required for the formation of the steady-state response [9]. In general, two stages of the response can be observed: 1) a transient *buildup* portion preceding and 2) a steady-state portion. In the steady-state portion, *ssVEPs* can be usually modeled as a linear combination of a fundamental frequency (usually the stimulator frequency) and its higher harmonics. However, such a model may not be sufficient to characterize the transient *VEP* (*rVEP*) portion immediately following stimulus onset.

Characterization of the transient portion may be best achieved in the time-frequency domain. The main advantage of this approach is to provide information about the time-course of the frequency content of the signal without the assumption of strict stationarity. This approach has proven to be beneficial to a number of problems of biomedical signal analysis [10], [11]. For EP analysis, in particular, one can identify three main categories of approaches: 1) application of the short-time Fourier transform (STFT) [7], [12], [13]; 2) wavelet transform [14]–[19]; and 3) matching-pursuit with Gabor logons [11], [20]–[23]. Although early application of the STFT was promising [7], [13], the use of fixed-width window analysis was put into question by a number of studies [12], [14], [24]. It was pointed out that components of relatively higher frequency and shorter duration were largely responsible for the earlier, transient components, while the later components are of lower frequency and longer duration. Therefore, an analysis with variable window length, such as the wavelet transform, will be more efficient for characterizing the entire signals given an appropriate choice of the mother wavelet. Indeed, the possibility of choosing the shape of wavelet to be similar to the signal under examination is one main advantage of wavelets over STFT. More recently, researchers have also been investigating the application of matching pursuit to EP estimation. In particular, matching pursuit with Gabor logon dictionary was applied to both *VEP* [21] and sleep EEG [22] analysis. The method of matching pursuit is “adaptive” and thus can lead to very compact representations of the signal. The adaptive procedure involves choosing a dictionary of functions which best matches the signal. Unlike wavelet analysis which is restricted by the constant- $Q$  property, the selected basis functions (i.e., logons) can be freely translated and scaled in the time-frequency plane allowing for true multi-resolution analysis.

We were inspired by the flexibility of this approach and have proposed the adaptive chirplet transform (ACT) [25] as an extension of existing work in this area. The essence of the ACT approach is to add an additional degree of freedom to Gabor logons by allowing them to rotate in the time-frequency plane. Thus, the signal’s energy distribution can now be approximated using time-frequency “tiles” with arbitrary slopes. When the entire signal is analyzed entirely without windowing or segmentation, this approach is referred to as the non-windowed ACT. One limitation of the non-windowed method comes from the difficulty in analyzing longtime signals. This is due to the time complexity of the analysis [26], which means that longer signals will incur a higher time cost. In situations where processing time is limited (e.g., in real-time applications), the non-windowed ACT approach may not be suitable.

To reduce computational time, the windowed ACT approach was proposed [27]. In this approach, the signal is partitioned into non-overlapping and equal length segments using rectangular truncation. A single chirplet is then estimated from each segment and hence the entire signal is approximated by a sequence of non-overlapping chirplets. In this paper, we describe the windowed ACT and apply it to investigate short-term changes in *VEPs*. We will show that both transient and steady-state portions of the response can be well characterized by a series of chirplets. A method for finding the optimal length of the window will also be discussed.

## II. COMPUTATIONAL APPROACH TO THE WINDOWED ACT

A Gaussian chirplet is a wave packet with a Gaussian envelope and four adjustable parameters [28]

$$g_{t_c, \omega_c, c, \Delta_t}(t) = \frac{1}{\sqrt{\pi \Delta_t}} \exp \left\{ -\frac{1}{2} \left( \frac{t - t_c}{\Delta_t} \right)^2 + j [c(t - t_c) + \omega_c] (t - t_c) \right\} \quad (1)$$

where  $j = \sqrt{-1}$ ,  $t_c$  is the time-center in seconds,  $\omega_c$  the frequency-center in radians,  $\Delta_t > 0$  the scale that is the effective time-spread in seconds, and  $c$  the chirp rate in radians per second that characterizes the “quickness” of frequency changes. The chirplet transform of a signal is defined as the inner product between the signal and the chirplet atom given in (1)

$$a_{t_c, \omega_c, c, \Delta_t} = \langle f, g_I \rangle = \int_{-\infty}^{\infty} f(t) g_{t_c, \omega_c, c, \Delta_t}^*(t) dt. \quad (2)$$

The coefficients  $a_{t_c, \omega_c, c, \Delta_t}$  reflect the similarity between the local structures of the signal and the chirplets. They represent the signal’s energy content in a time-frequency region specified by the chirplets. The set of chirplet parameters is denoted by a continuous index set  $I = (t_c, \omega_c, c, \Delta_t)$ .

The signal model consists of a weighted sum of chirplets plus noise

$$f(t) = \sum_{n=0}^{P-1} a_{I_n} g_{I_n}(t) + W(t) \quad (3)$$

where  $P$  is the number of chirplets and  $W(t)$  is a Gaussian white noise (GWN) with zero mean and variance  $\sigma^2$ . To estimate  $a_{I_n}$  and  $g_{I_n}$ , we previously proposed a coarse-refinement technique based on the matching-pursuit (MP) algorithm and the expectation-maximization (EM) algorithm. When a new chirplet is estimated with the MP algorithm, all previously estimated chirplets are progressively refined with the EM algorithm [25]. This non-windowed approach has been shown to be capable of characterizing both the short *rVEP* and long *ssVEP* portions successfully.

Since the computational cost of the non-windowed ACT is high, one can alternatively use a windowed approach [27]. With shorter data segments, the computational time can be significantly reduced. However, there is a tradeoff in terms of how much window length can be reduced while keeping relatively good time-frequency resolution for the estimation of local signal structures.

### A. Optimal Window Length

Generally speaking, the window length of data segment must be short enough for the chirplet to adequately “sample” the time-dependent behavior of the signal spectrum, yet minimize the error in the estimate. We will describe next the theoretical minimum variance for chirplet estimation and how the minimum window length can be obtained.

First, we focus on the lower bound of window length. In windowed ACT analysis, one and only one chirplet is estimated from each of the segment with the MP algorithm. Consequently, we use a single chirplet model to represent the windowed signal, i.e.,  $f(t) = a \cdot g(t) + W(t)$

TABLE I  
CRLBs OF THE CHIRPLET ESTIMATES

$\hat{\theta}$	$\hat{t}_c$	$\hat{\omega}_c$	$\hat{c}$	$\hat{\Delta}_t$	$\hat{\phi}$	$\hat{A}$	$\hat{\sigma}^2$
CRLB <sup>†</sup>	$\frac{\Delta_t^2}{\xi}$	$\frac{1 + 4c^2\Delta_t^4}{\xi\Delta_t^2}$	$\frac{4}{\xi\Delta_t^4}$	$\frac{\Delta_t^2}{2\xi}$	$\frac{3 + 4\omega_c^2\Delta_t^2}{4\xi}$	$\sigma^2$	$\frac{\sigma^4}{N}$

$$^\dagger \xi = A^2 / 2\sigma^2$$

and  $a = Ae^{-j\phi}$ . In the MP algorithm, the four estimates of the chirplet parameters are obtained from

$$\begin{bmatrix} \hat{t} \\ \hat{\omega}_c \\ \hat{c} \\ \hat{\Delta}_t \end{bmatrix} = \arg \max_{t_c, \omega_c, c, \Delta_t} |\langle f, g_I \rangle|^2 \quad (4)$$

where  $g_I$  is one of the predefined chirplets contained in the “dictionary” [29]. Subsequently, the estimated chirplet can be found by substituting (4) into (1). The other estimates are found by

$$\hat{A} = |\hat{z}|, \quad \hat{\phi} = -\angle \hat{z}, \quad \hat{\sigma}^2 = \frac{\|f\|^2 - |\hat{z}|^2}{2L} \quad (5)$$

where  $L$  is the size of  $f(t)$  and  $\hat{z} = \langle f, g \rangle$ . The minimum variance of these estimates is obtained by Cramér–Rao lower bounds (CRLBs) (Table I, cf. [26] for derivation).

The performance of the actual estimators was evaluated by computer simulation. The parameters of the model for simulation were  $A = 1$ ,  $\phi = 0$ ,  $t_c = L/2$ ,  $\omega_c = \pi/2$ ,  $c = \pi/L$ , and  $\Delta_t = 2$ , where the window length  $L$  varied from 24 to 1000 points. The variance of GWN  $\sigma^2$  was chosen so that the signal-to-noise ratio (SNR) of the simulated signal ranged from  $-20$  to  $20$  dB. The results are shown in Fig. 1, where the mean squared error (MSE) of the parameter estimates are compared with the CRLBs. Two general characteristics can be observed: one is that MSE approaches CRLB asymptotically for high SNR; the other is that MSE will converge to CRLB at lower SNR for longer window lengths. We have estimated the average SNR level of our data to be  $0.55 \pm 0.98$  dB, which is close to  $0$  dB. From Fig. 1, we see that at  $\text{SNR} = 0$  dB the MSE of the estimates follows the CRLB closely when the window length is no less than 100 points. Thus, to keep the estimator efficient, the window length should be no lower than 100 points. This determines the lower bound of the window length.

Next, we consider the upper bound on window length. A segment must be short enough to adequately sample the energy density curves of a signal in the time-frequency plane. Since most of the variation occurs in the transient, the choice of the upper bound will be mainly influenced by the time duration of the transient portion of the signal. Thus, we propose the following method to estimate the duration of  $r\text{VEP}$ : 1) reconstruct the  $r\text{VEP}$  signal from the chirplets extracted by the non-windowed ACT [25]; 2) find the envelope of the  $r\text{VEP}$ ; 3) locate the maximum of the envelope ( $A > 0$ ) and set a threshold of  $A/100$ ; 4) finally, define the duration time as the time interval between the instants at which the first point and the last point on the envelope exceeds the threshold. According to this procedure, we found that the average duration of our data is  $300 \pm 38$  points. Considering the lower limit imposed by the SNR condition, we therefore choose 100 points (416.7 ms at sampling rate of 240 Hz) to allow the highest possible time-resolution.

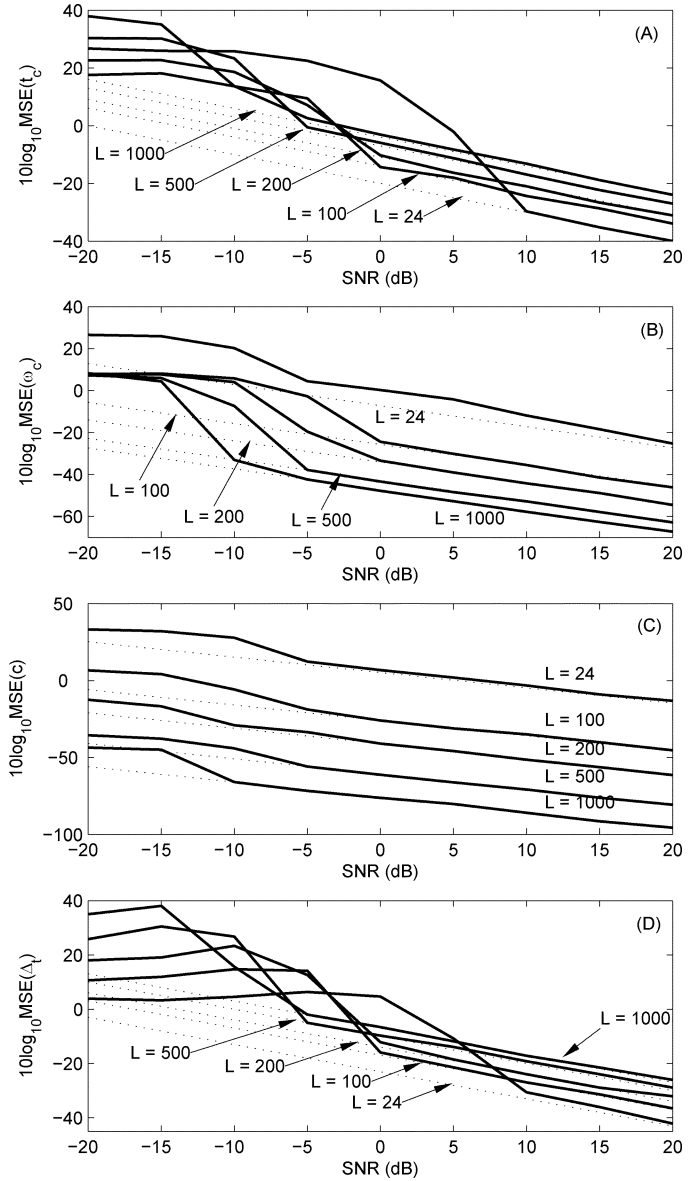


Fig. 1. Simulation results of estimating a single chirplet for different window lengths and SNR levels. In each figure, the dotted lines and solid lines are, respectively, the CRLBs and MSE of the estimates of corresponding estimators: (A) time-center ( $t_c$ ); (B) frequency-center ( $\omega_c$ ); (C) chirp rate ( $c$ ); and (D) time-spread ( $\Delta_t$ ).

### III. RESULTS AND DISCUSSION

As the details of the experimental setup have been reported elsewhere (e.g., [25]), we provide only a brief description here. Five adult subjects participated in the experiment. The visual stimulus consisted of a matrix of moving bars. All stimuli were presented on a LCD monitor. VEP signals were recorded via three gold-cup electrodes, including the active electrode placed on the scalp at the  $O_z$  position, the reference one placed on the left ear lobe and the third one attached to right ear lobe serving as the ground. The signals were amplified ( $1000\times$ ), bandpass filtered ( $0.01\text{--}40$  Hz), and passed through an analog-to-digital (A/D) converter (sampled at 240 Hz) before being streamed to the harddisk. The data were then processed offline to obtain five averaged signals (denoted as  $D_1\text{--}D_5$ , 1200 points each).

Subsequently, each signal was divided into twelve 100-point segments to “extract” one chirplet from each segment, resulting in 12 chirplet atoms. The results of the windowed ACT can be visualized

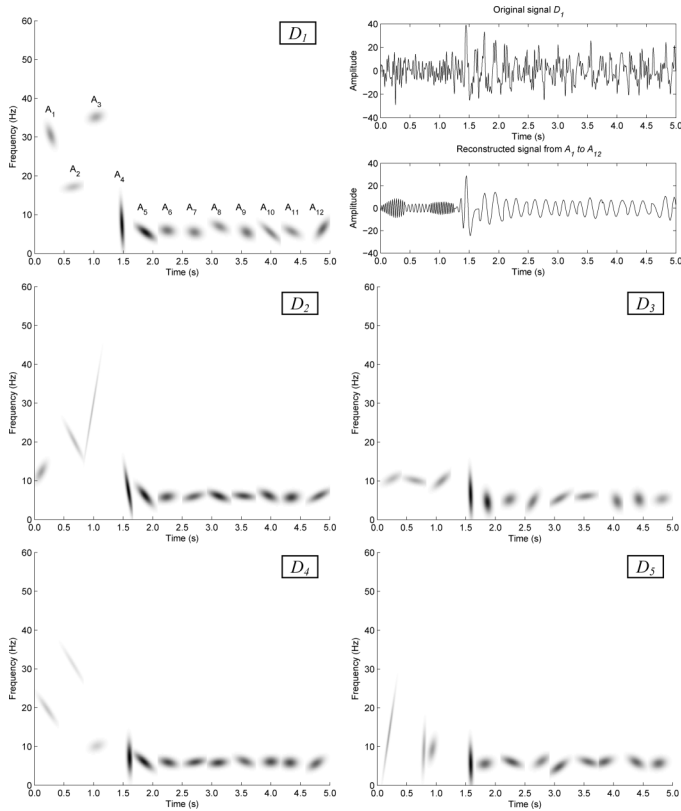


Fig. 2. Time-frequency structures of signals  $D_1$ – $D_5$ . For each signal, 12 chirplet atoms have been estimated, which are labeled as  $A_1$ – $A_{12}$  (shown in panel  $D_1$ ). As an example, the original signal  $D_1$  and the reconstructed signal are shown on the right.

with Wigner–Ville distributions (WVDs). The visualization of the estimated atoms of all five signals  $D_1$ – $D_5$  are shown in Fig. 2, where the atoms are labeled as  $A_1$ – $A_{12}$  (shown in panel  $D_1$ ). The results show a similar pattern, i.e., the signal before 1.25 s is represented by three atoms,  $A_1$ – $A_3$  with lower amplitudes and higher frequency centers, followed by two atoms with relatively stronger amplitudes and shorter time-spreads. Their chirp rates are generally negative, indicating downward transition of the instantaneous frequencies. The rest of the signal is represented by a series of seven atoms denoted by  $A_6$ – $A_{12}$ . Most of them have wide time-spreads and small chirp rates. Their frequency-centers are close to 6 Hz. These observations regarding the VEP variation can be further confirmed by the statistics of the estimates (see Fig. 3). For the sake of clarity, the standard deviations (SD) of the estimates are not shown in the figure, but summarized in Table II instead. In panel (A), it can be seen that a clear transition of central frequencies can be observed between  $A_3$  and  $A_4$ . In particular, the chirp rate of  $A_4$  is a large negative value, indicating a sharp decrease in instantaneous frequency. The frequency-centers of rest chirplets are close to 6 Hz and their chirp rates are close to zero. In panel (B), a prominent character is that  $A_4$  acquires significantly shorter time-spread and higher amplitude.

Moreover, we demonstrate the efficacy of the windowed ACT approach by comparing it with the results from four other methods of time-frequency analysis. Fig. 4 shows the time-frequency structures of signal  $D_1$  estimated with: (A) STFT; (B) WVD; (C) reduced interference distribution (RID) [11]; and (D) the non-windowed ACT [25], respectively. Although the spectrogram based on the STFT can show some of the salient time-frequency structures, most of the details are lost due to smearing. In panel (A), for instance, a major structure with

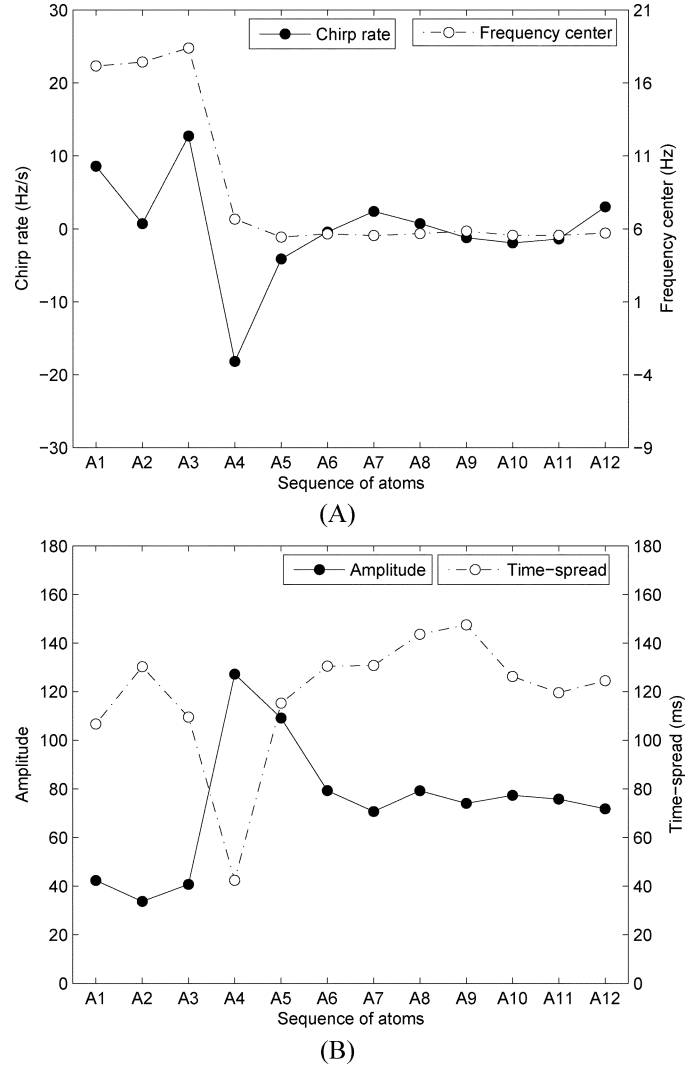


Fig. 3. Averaged parameters for the atoms  $A_1$ – $A_{12}$ . (A) Average chirp rates and frequency-centers. (B) Average amplitudes and time-spreads.

TABLE II  
STANDARD DEVIATIONS (SD) OF THE PARAMETER ESTIMATES OF CHIRPLETS, INCLUDING CHIRP RATE ( $c$ ), FREQUENCYCENTER ( $f_c$ ), AMPLITUDE ( $a$ ), AND TIME-SPREAD ( $\Delta_t$ )

Atoms	SD( $c$ ) (Hz/s)	SD( $f_c$ ) (Hz)	SD( $a$ )	SD( $\Delta_t$ ) (s)
$A_1$	24.66	8.14	16.76	30.07
$A_2$	17.66	8.96	12.31	56.25
$A_3$	18.93	12.18	15.06	24.99
$A_4$	11.58	0.79	23.90	10.09
$A_5$	3.12	0.69	30.47	28.54
$A_6$	1.69	0.35	11.58	16.16
$A_7$	2.83	0.62	11.78	27.92
$A_8$	3.40	0.80	12.39	11.87
$A_9$	1.32	0.29	12.17	24.45
$A_{10}$	3.03	0.63	7.71	22.28
$A_{11}$	1.67	0.29	5.76	16.99
$A_{12}$	2.24	0.43	20.73	20.23

relatively constant frequency below 10 Hz is observable. However, it is difficult to tell more precisely the value of the constant frequency and the details of variation at the beginning of the response. The WVD representation of the signal in (B), on the other hand, provides a result with much higher time-frequency resolution. Unfortunately, WVD suffers from the interference (cross-terms) from interactions between signal

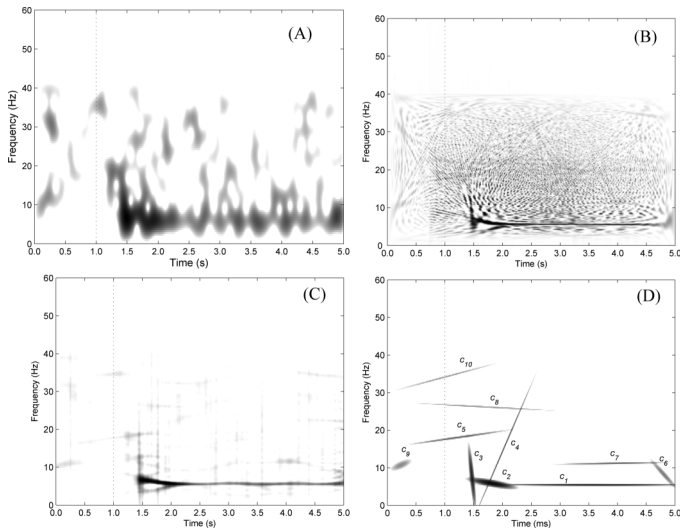


Fig. 4. Comparison of four time-frequency representations of signal  $D_1$ . (A) STFT (with 11-point Gaussian window). (B) WVD. (C) RID (with Hanning kernel). (D) Non-windowed ACT.  $c_1$ – $c_{10}$  denote the ten extracted chirplets [25]. The dotted line at 1 s indicates the onset of the visual stimuli.

components themselves, and between signal components and noise. The resulting visualization is usually fuzzier and hence confusing. A tradeoff, however, can be achieved by using the representation based on RID, as is shown in (C). The interference has been effectively suppressed at the expense of time-frequency resolution. This approach can usually lead to a clearer visualization. As shown in panel  $D_1$  of Fig. 2, such an effect of a clear display can also be achieved reasonably well by the windowed ACT since it plots WVD of single chirplet in each segment and is thus free of interference. It can be seen that all of these four representations are capable of capturing the transient portion of the VEP with downward instantaneous frequency components within the first second period posterior to stimulus onset. However, we note that the windowed approach can offer a succinct and compact representation by characterizing it with two chirplets ( $A_4$  and  $A_5$ ) involving only ten parameters. These parameters may be employed as signal features in the tasks of pattern recognition or data compression. In contrast, the approaches of the STFT, WVD, and RID, represent the transient VEP with hundreds of coefficients. A compact representation using chirplets can also be used to readily reconstruct the transient signal in the time domain (shown in Fig. 2), which may not be easily achieved by the other three methods.

Although the non-windowed approach of ACT will give a more compact representation of the VEP [panel (D) of Fig. 4], it should be noted that the non-windowed ACT demands much more computational time than its windowed counterpart. In practice, the non-windowed ACT also requires the entire signal before commencing analysis. The windowed method, on the other hand, reduces waiting time by collecting just one data segment, which is more suitable for the situations of real-time processing.

Finally, we conclude from the previous results and discussions that the estimated chirplets by windowed ACT reveals a similar pattern of VEP response shown by the non-windowed method [25]. The windowed approach will find applications where fast time computation and longtime signal monitoring are necessary.

## REFERENCES

[1] D. Regan, *Human Brain Electrophysiology: Evoked Potentials and Evoked Magnetic Fields in Science and Medicine*. New York: Elsevier, 1989.

[2] A. M. Halliday, *Evoked Potentials in Clinical Testing*. Edinburgh, Scotland: Churchill Livingstone, 1993.

[3] G. B. Arden and J. R. Heckenlively, *Principles and Practice of Clinical Electrophysiology of Vision*. St. Louis: Mosby Year Book, 1991.

[4] J. R. Wolpaw, N. Birbaumer, D. J. McFarland, G. Pfurtscheller, and T. M. Vaughan, "Brain-computer interfaces for communication and control," *Clinical Neurophys.*, vol. 113, pp. 767–791, 2002.

[5] M. Cheng, X. R. Gao, S. G. Gao, and D. F. Xu, "Design and implementation of a brain-computer interface with high transfer rates," *IEEE Trans. Biomed. Eng.*, vol. 49, no. 10, pp. 1181–1186, Oct. 2002.

[6] W. A. Ho and M. A. Berkley, "Evoked-potential estimates of the time course of adaptation and recovery to counterphase gratings," *Vision Res.*, vol. 28, pp. 1287–1296, 1988.

[7] N. S. Peachey, P. J. Demarco, R. Ubilluz, and W. Yee, "Short-term changes in the response characteristics of the human visual-evoked potential," *Vision Res.*, vol. 34, pp. 2823–2831, 1994.

[8] D. Y. Xin, W. Seiple, K. Holopigian, and M. J. Kupersmith, "Visual-evoked potentials following abrupt contrast changes," *Vision Res.*, vol. 34, pp. 2813–2821, 1994.

[9] L. H. Van Der Tweel, "Relation between psychophysics and electrophysiology of flicker," *Documenta Ophthalmologica*, vol. 18, pp. 287–304, 1964.

[10] Z. Y. Lin and J. D. Chen, "Advances in time-frequency analysis of biomedical signals," *Critical Rev. Biomed. Eng.*, vol. 24, pp. 1–72, 1996.

[11] M. Akay and I. E. i. M. a. B. Society, *Time-Frequency and Wavelets in Biomedical Signal Processing*. Piscataway, NJ: IEEE Press, 1998.

[12] J. P. C. Deweerdt and J. I. Kap, "Spectro-temporal representations and time-varying spectra of evoked-potentials – A methodological investigation," *Biological Cybern.*, vol. 41, pp. 101–117, 1981.

[13] A. M. Norcia, T. Sato, P. Shinn, and J. Mertus, "Methods for the identification of evoked-response components in the frequency and combined time frequency domains," *Electroencephalography Clinical Neurophys.*, vol. 65, pp. 212–226, 1986.

[14] L. J. Trejo and M. J. Shensa, "Feature extraction of event-related potentials using wavelets: An application to human performance monitoring," *Brain Lang.*, vol. 66, pp. 89–107, 1999.

[15] Z. Zhang, H. Kawabata, and Z.-Q. Liu, "Electroencephalogram analysis using fast wavelet transform," *Comput. Biol. Med.*, pp. 429–440, 2001.

[16] O. Bertrand, J. Bohorquez, and J. Pernier, "Time-frequency digital filtering based on an invertible wavelet transform—An application to evoked-potentials," *IEEE Trans. Biomed. Eng.*, vol. 41, pp. 77–88, 1994.

[17] R. Q. Quiroga, O. W. Sakowitz, E. Basar, and M. Schürmann, "Wavelet transform in the analysis of the frequency composition of evoked potentials," *Brain Res. Protocols*, pp. 16–24, 2001.

[18] N. V. Thakor, X. R. Guo, Y. C. Sun, and D. F. Hanley, "Multiresolution wavelet analysis of evoked-potentials," *IEEE Trans. Biomed. Eng.*, vol. 40, no. 11, pp. 1085–1094, Nov. 1993.

[19] N. V. Thakor, X. R. Guo, C. A. Vaz, P. Laguna, R. Jane, P. Caminal, H. Rix, and D. F. Hanley, "Orthonormal (Fourier and Walsh) models of time-varying evoked-potentials in neurological injury," *IEEE Trans. Biomed. Eng.*, vol. 40, no. 3, pp. 213–221, Mar. 1993.

[20] P. J. Durka and K. J. Blinowska, "Analysis of EEG transients by means of matching pursuit," *Annals. Eng.*, vol. 23, pp. 608–611, 1995.

[21] M. L. Brown, W. J. Williams, and A. O. Hero, "Non-orthogonal Gabor representations of biological signals," in *Proc. IEEE Int. Conf. Acoust., Speech Signal Process.*, 1994, pp. 305–308.

[22] K. J. Blinowska and P. J. Durka, "Unbiased high resolution method of EEG analysis in time-frequency space," *Acta Neurobiologiae Experimentalis*, vol. 61, pp. 157–174, 2001.

[23] P. J. Durka, "From wavelets to adaptive approximations: Time-frequency parametrization of EEG," *Biomed. Eng. Online*, vol. 2, p. 1, 2003.

[24] S. J. Schiff, A. Aldroubi, M. Unser, and S. Sato, "Fast wavelet transformation of EEG," *Electroencephalography Clinical Neurophys.*, vol. 91, pp. 442–455, 1994.

[25] J. Cui and W. Wong, "The adaptive chirplet transform and visual evoked potentials," *IEEE Trans. Biomed. Eng.*, vol. 53, no. 7, pp. 1378–1384, Jul. 2006.

[26] J. Cui, "Adaptive chirplet transform for the analysis of visual evoked potentials," Ph.D. dissertation, Inst. Biomater. Biomed. Eng., Univ. Toronto, Toronto, ON, Canada, 2006.

[27] J. Cui, W. Wong, and S. Mann, "Time-frequency analysis of visual evoked potentials using chirplet transform," *Electron. Lett.*, vol. 41, pp. 217–218, 2005.

- [28] S. Mann and S. Haykin, "The chirplet transform—Physical considerations," *IEEE Trans. Signal Process.*, vol. 43, no. 11, pp. 2745–2761, Nov. 1995.
- [29] S. G. Mallat and Z. Zhang, "Matching pursuit with time-frequency dictionaries," *IEEE Trans. Signal Process.*, vol. 41, no. 12, pp. 3397–3415, Dec. 1993.

## The Influence of CSF on EEG Sensitivity Distributions of Multilayered Head Models

K. Wendel, *Student Member, IEEE*, N. G. Narra, M. Hannula, P. Kauppinen, and J. Malmivuo, *Fellow, IEEE*

**Abstract**—We examined how the cerebrospinal fluid (CSF) affects the distribution of electroencephalogram (EEG) measurement sensitivity. We used concentric spheres and realistic head models to investigate the difference between computed-tomography (CT) and magnetic resonance image (MRI) models that exclude the CSF layer. The cortical EEG sensitivity distributions support these phenomena and show that the CSF layer significantly influences them, thus identifying the importance of including the CSF layer inside the head volume conductor models. The results show that the highly conductive CSF channels the current, thus decreasing the maximum cortical current density relative to models that do not include the CSF. We found that the MRI and CT models yielded HSV results 20% and 45%, respectively, too small when compared with CSF-inclusive models.

**Index Terms**—Conductivity, cerebrospinal fluid (CSF), electroencephalogram (EEG), lead field current density, sensitivity distribution, volume conductor.

### I. INTRODUCTION

Traditionally head models have been constructed as three concentric spheres [1]–[3], modeling the scalp, skull, and brain. Recently, realistic models are constructed from a set of segmented image slices, usually originating from one of the primary medical imaging modalities—computed tomography (CT) or magnetic resonance images (MRI). Considering their pros and cons, CT more accurately images the skull due to its sensitivity to hard tissue, whereas MRI better images soft tissues such as the skin, cortex, and the gray matter-white matter boundary [4]. The differences between the three-layer CT- and MRI-based models in [4] illustrate significant differences at the base of the skull.

The cerebrospinal fluid (CSF) layer, which surrounds the brain, is often neglected either due to the difficulty to correctly segment this layer from T1- and T2-weighted MRIs [5] or the insensitivity of CT images to soft tissues. The omission of the CSF layer can alter the segmentation via incorporation into the skull or into the brain (gray matter). Some realistic head models explicitly define the skull as the region between the scalp and the cortex, whereas, other models define the brain as the region inside the skull [4]. MRI-based models by Ramon

*et al.* [5] include the CSF layer and indicate the significance this layer has on scalp potentials and on the inverse source localizations.

By incorporating CSF in one type of head model and removing it from the other two, we examine the role of CSF and how it affects the images of the two modalities that do not directly include this layer. We use both spherical and realistic models to investigate the sensitivity distributions. In this work, we construct head models representing a matched MRI-CT- (i.e., CSF inclusive), MRI-, and a CT-based model. These models identify the significance of including the CSF layer inside the head volume conductor model by studying how electrode separation affects the cortical sensitivity distributions.

### II. METHODS

#### A. Model Geometries

We used spherical models to illustrate the general results and to reveal the underlying phenomena. We modeled four concentric spheres with radii of 7.45, 7.80, 8.45, and 9.0 cm for the brain, CSF, skull, and scalp, respectively [6]–[8]. We use realistic models to validate the spherical model findings. We segmented the Visible Human Woman (VHW) from the Visible Human Project [9] since tissue segmentation eliminates the MRI-CT data set registration. These models are constructed by addressing the tissues separately. Each tissue was segmented, slice contoured, and lofted together.

In both the spherical and realistic sets, the three-layer CT-model defines the brain as the region inside the interior skull boundary; the three-layer MRI-model defines the skull as the region between the skull exterior and the brain exterior; the four layer CSF-model defines the CSF as the layer between the skull interior and the brain exterior. A fourth set, the three-layer CT2 model, is based on the CT-model results but excludes the cortical results that lie outside the actual brain exterior (i.e., the CSF). Finally, we calculate the CT2 sensitivity volumes and maximum current density values from only the volume contained by the actual brain.

We spaced all electrodes between 10° and 40° apart. Furthermore, we calculated that the smallest adjacent bipolar lead pair of the 256-, 128-, 64-, and 32- channel electroencephalogram (EEG) electrode montages is represented by spherical angles 11°, 18°, 23°, and 31°, respectively. We fitted our spherical angles according to standard EEG nomenclature [10]. We modeled all electrodes as 3-D simple recessed electrodes [11] with radii of 5 mm, corresponding to the size of high-resolution EEG caps [3]. Since the analytical model solves for the point electrode [12], we constructed finite-element method models and meshed them with tetrahedral adaptive meshes via COMSOL Multiphysics, COMSOL Group, Sweden.

#### B. Sensitivity Distribution Simulations

We simulated the sensitivity distributions through a range of tissue conductivities. We modeled the brain, CSF, and scalp compartments as 0.25, 1.79, and 0.45 S/m, respectively [13], [7]. The skull was modeled using brain-to-skull conductivity ratios  $\sigma_{Br}/\sigma_{Sk}$  of 5, 10, 15, 20, and 80 according to [14]. The sensitivity distributions are calculated according to the current density  $\mathbf{J}$ , where

$$\mathbf{J} = -\sigma \nabla \Phi + \mathbf{J}^e \quad (1)$$

is a function of the scalar potential  $\Phi$  and the externally applied current density  $\mathbf{J}^e$ , assuming bioelectric currents and voltages to be quasi static [6]. We fed a 1 A reciprocal current into a source electrode flowing to a grounded electrode. The distribution of the current in the model maps the lead field, i.e., the measurement sensitivity distributions. We

Manuscript received March 12, 2007; revised September 4, 2007. This work was supported by the Finnish Funding Agency for Technology and Innovation (TEKES), the Ragnar Granit Foundation, and the International Graduate School of Biomedical Engineering and Medical Physics, Finland. Asterisk indicates corresponding author.

\*K. Wendel is with the Ragnar Granit Institute, Department of Electrical Engineering, Tampere University of Technology, 33101 Tampere, Finland (e-mail: katrina.wendel@tut.fi).

N. G. Narra, M. Hannula, P. Kauppinen, and J. Malmivuo are with the Ragnar Granit Institute, Department of Electrical Engineering, Tampere University of Technology, 33101 Tampere, Finland.

Digital Object Identifier 10.1109/TBME.2007.912427